Structural Design of a Bionic Bone-Contraction Variable-Diameter Pipeline Robot

Wenxuan Yu[1,*], Chaoran Hu[1]
[1]College of Mechanical and Electrical Engineering, China University of Petroleum (East China), Qingdao, 266580, China
Corresponding author: Wenxuan Yu (e-mail: 197141ywx@gmail.com).

ABSTRACT To improve the adaptability and structural efficiency of pipeline robots in small and medium variable-diameter pipelines, a bionic bone-contraction variable-diameter pipeline robot is proposed. The so-called bone-contraction mechanism is an engineering abstraction of feline shoulder-thorax compliance rather than literal bone shortening: the cat scapula is mainly constrained by muscle-ligament tissues and can slide relative to the thoracic wall, allowing the effective body width to decrease when passing through narrow gaps. This biological mechanism is transformed into a six-leg radial support system composed of a flexible spine, spherical/universal joints and spring-preloaded support legs. Static and dynamic models are established for diameter-changing conditions, and the main load-bearing components are verified by finite element analysis and SIMP-based topology optimization. The main innovations are: a biologically consistent shoulder-thorax-to-flexible-spine mapping, an active-passive variable-diameter support principle, a theoretical model for contact force, spring preload, driving torque and energy consumption, and a topology-based structural weight-reduction scheme. The robot can adapt to pipe diameters of 200–440 mm. Under the worst working condition, the maximum Von-Mises stress is 186.4 MPa and the first-order natural frequency is 42.6 Hz. After topology optimization, the main-frame mass decreases from 2.84 kg to 2.17 kg, corresponding to a 23.7% reduction relative to the initial frame of the proposed robot. This result is defined as within-design structural weight reduction rather than a claim of product-level lightweight superiority over a commercial robot. The results provide a feasible route for adaptive cleaning and inspection robots in variable-diameter pipelines.

INDEX TERMS Variable-diameter pipeline robot, Bionic bone-contraction mechanism, Dynamic modeling, Finite element analysis, Topology-based weight reduction

I. INTRODUCTION

PIPELINE systems are widely used in urban drainage, water supply, petrochemical transportation and natural gas networks. Small and medium pipelines with diameters of 200–440 mm account for a large proportion of municipal pipe networks, while scaling, corrosion, deposition and local blockage reduce flow capacity and maintenance safety. Conventional cleaning methods, such as high-pressure water jetting and pigging, are limited when pipelines contain abrupt diameter transitions, elbows or local obstacles. Therefore, compact robots capable of adaptive support and stable movement in variable-diameter pipelines are required. Studies on wheel-leg, support, inspection and tracked pipeline robots provide the engineering background for this requirement [1], [2].

Existing pipeline robots can be classified by driving mode into fluid-driven, wheeled, tracked, screw-driven, peristaltic, supporting and legged types [3]–[5]. Recent international studies have further reported millimeter/sub-centimeter pipeline robots, untethered worm-inspired soft robots and large-diameter inspection platforms, demonstrating progress in miniaturization, compliance and field deployment [6]–[8]. Wheeled and tracked robots have high driving efficiency but poor passability in diameter-changing sections. Supporting and screw-driven robots can generate larger contact forces, but local rigid collision and energy consumption may increase under abrupt diameter variation. Bionic and soft mechanisms improve environmental adaptability, yet many studies focus on motion realization rather than the quantitative coupling between support force, pipe-wall contact, structural strength and lightweight design [9], [10].

The current studies still show five limitations. First, the radial support force and spring preload of the variable-diameter mechanism are often simplified, resulting in insufficient guidance for spring and motor selection. Second, the necessity of bionic design is sometimes stated only as a morphological analogy, without clarifying what biological structure is imitated and what mechanical benefit is obtained. Third, the adaptive principle of a pipeline robot in diameter transition sections is often described qualitatively, while the coordinated process among radial contraction, spring compliance, universal-joint compensation and pipe-wall contact is not fully explained. Fourth, finite element verification is sometimes presented as a process description, without mesh independence, material basis, boundary-condition explanation or resonance evaluation. Fifth, many papers use the term lightweight broadly; however, true product-level lightweighting should be benchmarked against mature commercial or deployed designs. In this study, the reported mass reduction is therefore limited to a comparison between the initial and optimized structures of the proposed robot, while product-level benchmarking is identified as future work [11].

To address these limitations, this paper conducts structural design, theoretical modeling, finite element verification and topology-based structural weight reduction for a bionic bone-contraction variable-diameter pipeline robot. The main innovations and contributions are summarized as follows:

(1) a cat-inspired bone-contraction support concept is proposed, in which feline shoulder-thorax compliance is converted into a flexible-spine and universal-joint support architecture instead of being treated as a simple appearance imitation;

(2) an active-passive coordinated variable-diameter mechanism is developed, where servo-driven radial leg adjustment provides large-stroke adaptation and spring preload provides local passive compliance;

(3) the adaptive pipe-passing principle is clarified through the sequence of contact establishment, radial contraction, self-centering and elastic recovery, which explains how the robot maintains contact in 200–440 mm pipes;

(4) static and dynamic models are established for support force, spring preload, driving torque and energy consumption; and

(5) topology-based weight reduction is carried out with an explicitly defined scope, namely within-design structural optimization rather than absolute comparison with a mature commercial product. The research object and bionic inspiration are summarized in Figure 1.

II. STRUCTURAL DESIGN AND THEORETICAL MODELING

A. BIONIC MECHANISM AND STRUCTURAL COMPOSITION

The robot consists of a central control cabin, six radially distributed support legs, a flexible spine connection, a drive transmission module and a rotary cleaning unit, as shown in Figure 1 and Figure 2. The support legs are arranged at 60° intervals around the central axis, and the end of each leg is equipped with an elastic contact pad to increase traction and reduce rigid collision with the pipe wall. Active servo actuation adjusts the radial position of the legs, whereas the preloaded spring provides passive compliance when the local pipe diameter changes abruptly [12]–[15].

In this study, the term “bone-contraction” does not mean that feline bones physically shorten. It refers to the apparent reduction of the effective body width when a cat passes through a narrow space. The key biological reason is that the cat shoulder girdle has a highly compliant connection to the thorax: the scapula can slide along the thoracic wall under the constraint of muscles and ligaments, the forelimbs can rotate and retract, and the spine provides additional bending compliance. As a result, the animal can redistribute contact force and reduce local impact without losing support. This mechanism is suitable for pipeline robots because a variable-diameter pipe imposes similar requirements: the robot must shrink its radial envelope, maintain sufficient normal force and avoid rigid collision at elbows or diameter transitions.

The necessity of the bionic design lies in the conflict between support stability and diameter adaptability. A purely rigid support mechanism can generate traction in a constant-diameter pipe, but at diameter transitions the normal force changes abruptly, which may cause wheel slip, impact loading, increased motor torque and stress concentration at the support-arm root. The proposed bionic support transfers this conflict into an active-passive compliant mechanism: the flexible spine accommodates axial bending and small posture errors, the spherical/universal joints compensate angular misalignment between the support legs and the pipe wall, and the spring-preloaded legs maintain a controllable normal force during radial contraction and expansion. Therefore, the bionic feature provides a functional benefit: it improves self-centering, impact buffering, contact-force continuity and passage stability in variable-diameter pipes.

To strengthen bionic consistency, the feline shoulder-thorax compliance is quantitatively mapped to robot modules in Table 1. In cats, the scapula is not rigidly locked to the sternum; instead, muscle-ligament connections allow sliding, rotation and elastic buffering. In the robot, these biological functions are realized by the flexible spine, spherical/universal joints, radial guide/support legs and preloaded springs. The mapping clarifies how the bionic idea is implemented mechanically: the flexible spine corresponds to axial compliance, the universal joint corresponds to multi-directional angular compensation, the spring corresponds to muscle/ligament elasticity, and the radial legs correspond to the reduction of the effective body envelope. The engineering objective is to maintain a stable contact force of 5.40–5.77 N over a 200–440 mm pipe-diameter range without using a fully rigid support frame.

The pipe-adaptation process can be divided into three stages. First, in a large-diameter section, the six support legs extend radially and establish multi-point contact with the pipe wall; the 60 deg circumferential arrangement generates a self-centering effect and prevents the body from leaning to one side. Second, when the robot enters a smaller or locally narrowed pipe, the contact force at the leg ends increases; the springs are compressed and the universal joints rotate

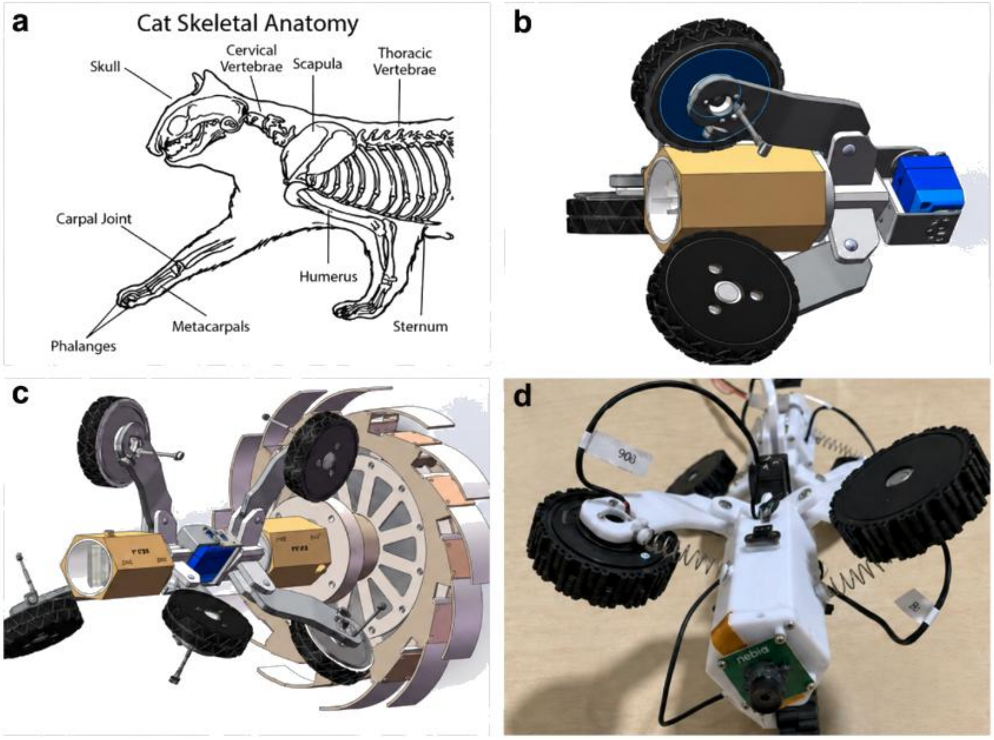

FIGURE 1. Bionic inspiration and prototype of the variable-diameter pipeline robot. (a) Cat skeletal anatomy and shoulder-thorax compliance. (b) Bionic bone-contraction support structure. (c) SolidWorks assembly model. d, Physical prototype.

TABLE 1. Expanded Biological-To-Mechanical Mapping Of The Bionic Bone-Contraction Mechanism.

Biological characteristic	Mechanical translation	Functional role	Quantitative/design index
Scapula-thorax connection by muscles/ligaments	Flexible spine + spherical/universal joint	Multi-DOF compliance and bend adaptation	Six legs distributed at 60 deg intervals
Muscle/ligament elasticity	Spring preload in each support leg	Stable pipe-wall contact and impact buffering	Preload: 5.07–5.42 N
Thoracic profile variation during narrow-space passage	Radial variable-diameter support mechanism	Adaptive passage in diameter-changing pipes	Pipe diameter: 200–440 mm
Soft paw contact and friction regulation	Elastic pad and rotary cleaning unit	Traction, cushioning and wall-cleaning stability	Contact force: 5.40–5.77 N
Sliding motion of scapula along thoracic wall	Radial guide path + hinge/universal joint	Allows support-leg angular compensation during diameter change	Radial contraction from 440 mm to 200 mm
Forelimb retraction during narrow-space passage	Servo-driven radial leg retraction	Reduces the external envelope before entering a smaller pipe	Active diameter adjustment stroke matched to 200–440 mm pipes
Distributed limb support and body self-centering	Six-leg circumferential support layout	Balances pipe-wall normal forces and prevents eccentric jamming	Leg spacing: 60 deg; six-point radial support

to absorb angular error, while the servo system retracts the support legs to reduce the outer envelope. Third, after passing the transition section, the spring preload drives the legs to recover contact and the control system restores the required support radius. This active-passive process is the mechanical implementation of the feline bone-contraction inspiration and is the reason why the robot can adapt to 200–440 mm pipes instead of only moving in a fixed diameter [16]–[18].

Compared with a purely wheeled or rigid supporting robot, the proposed mechanism has four expected advantages in variable-diameter pipelines:

(1) the support radius can be actively adjusted according to pipe diameter;

(2) the spring preload reduces sudden impact when the pipe diameter changes;

(3) the universal joint prevents side loading caused by non-coaxial contact; and

(4) the six-leg layout distributes the normal force, thereby improving traction and reducing local pipe-wall pressure.

These advantages directly support the cleaning and inspection tasks in municipal pipes with elbows, deposits, diameter changes and local obstacles. Representative structural views retained from the original SolidWorks model are integrated in Figure 2. After removing redundant views, the retained panels show the end support and pipe-wall contact module, the transmission connection between modules, and the enlarged elastic cleaning blade assembly. These struc-

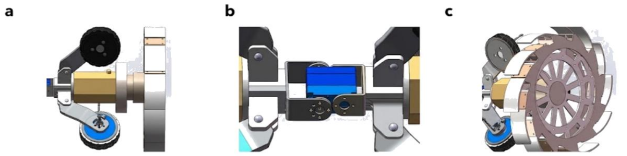

FIGURE 2. Selected structural details retained from the original SolidWorks model. (a) End support and wheel/pipe-wall contact module. (b) Transmission connection between modules. (c) Enlarged view of the elastic cleaning blade assembly.

tures correspond to the support, transmission and cleaning functions of the robot, respectively. In particular, the end support module provides radial contact, the transmission module transfers the driving torque under changing posture, and the elastic blade assembly maintains cleaning contact when the body radius changes.

B. KINEMATIC AND STATIC EQUILIBRIUM MODEL

For a circular pipe with inner diameter D, let r_0 be the equivalent radius of the central body, l be the extension length of one support leg and θ be the angle between the support leg and the local radial direction. The simplified kinematic relation is given by Eq. (1). In accordance with common mathematical-symbol rules, scalar variables are treated as italic quantities, standard functions such as cos are upright operators, and units are written in roman type [19], [20].

$$l(D,\theta) = \frac{D/2 - r_0}{\cos\theta} \tag{1}$$

Equation (1) shows that the required support-leg extension is directly governed by the pipe diameter. When D decreases, the radial distance between the pipe wall and the robot body decreases, so the support leg must retract; when D increases, the leg extends again to maintain contact. The flexible spine and universal joints do not change this geometric relation, but they reduce the angular error θ and prevent the radial support from becoming an over-constrained rigid contact. Therefore, the bionic structure improves adaptability by combining geometric diameter adjustment with compliant force regulation.

The model assumes that the pipe cross-section is circular, the robot moves quasi-statically during diameter adjustment, the six legs are symmetrically distributed, and the contact pad obeys a Coulomb friction model. For the i-th support leg, the normal contact force is N_i, the support angle is ϕ_i, the spring force is F_s, the spring stiffness is k, the spring compression is δ and the friction coefficient is μ. The static balance and driving conditions are expressed by Eqs. (2) to (5).

TABLE 2. Key theoretical parameters under variable pipe-diameter conditions.

Parameter	$D = 440$ mm	$D = 200$ mm	Unit
Support angle	15	25	deg
Single-leg contact force	5.40	5.77	N
Spring preload	5.07	5.42	N
Driving torque	2.84	3.76	N m
Spring compression	12.8	8.6	mm

$$\sum_{i=1}^{n} N_i \cos\phi_i = mg \tag{2}$$

$$F_d \le \mu \sum_{i=1}^{n} N_i \tag{3}$$

$$F_s = k\delta + F_0, \quad N_i = F_s \cos\beta_i \tag{4}$$

$$T_m \ge \sum_{i=1}^{n} (\mu N_i r_{e,i}) + T_r \tag{5}$$

where F_d is the axial resistance, T_m is the minimum motor torque, $r_{e,i}$ is the effective contact radius and T_r is the internal transmission resistance. Using a total mass of 3.2 kg and six radial support legs, the theoretical parameters under the maximum and minimum pipe-diameter conditions are obtained in Table 2.

C. DYNAMIC STABILITY AND ENERGY-CONSUMPTION MODEL

The above formulation describes the quasi-static support requirement. When the robot passes through an inclined or curved variable-diameter section, radial leg extension, body translation and pipe-wall friction become dynamically coupled. Therefore, the generalized coordinate is defined as $q = [x, \psi, l_1, \ldots, l_n]^T$, where x is the axial displacement, ψ is the body attitude angle and l_i is the radial extension of the i-th support leg. The Lagrange equation in Eq. (6) is introduced to describe this coupling.

$$\frac{d}{dt}\frac{\partial L}{\partial \dot{q}_j} - \frac{\partial L}{\partial q_j} = Q_j, \quad j = 1, 2, \ldots, n+2 \tag{6}$$

where $L = T - V$ is the Lagrangian, and Q_j represents motor torque, friction and pipe-wall reaction. The compact dynamic equation can be written as Eq. (7).

$$M(q)\ddot{q} + C(q,\dot{q})\dot{q} + K_s(q - q_0) + G(\alpha) + R_c = \tau \tag{7}$$

where $M(q)$ is the inertia matrix, $C(q,\dot{q})$ is the velocity coupling term, K_s is the equivalent spring stiffness matrix, $G(\alpha)$ is the gravity component on an inclined pipe with slope angle α, R_c is the contact/friction resistance and τ is the generalized driving input. This formulation indicates that dynamic stability is improved when the radial support force changes smoothly and when the inertia of the main frame is reduced. The energy consumed during the diameter-changing process can be estimated by the motor work, friction work and radial compliance loss, as given in Eq. (8).

$$E = \int_0^t \left[T_m\omega_m + \sum_{i=1}^{n} \mu N_i |\dot{x}| + \sum_{i=1}^{n} c_i l_i^2 \right] dt \tag{8}$$

TABLE 3. Mesh-independence verification of the finite element model.

Element size (mm)	5.0	4.0	3.0	2.5
Max stress (MPa)	181.7	184.9	186.4	187.1
Max deformation (mm)	0.506	0.519	0.523	0.526

In this model, lightweight optimization reduces the inertia term in $M(q)$ and the required motor work $T_m\omega_m$. The measured design indicator is expressed as

$$\eta_p = \frac{P_0 - P_{\text{opt}}}{P_0} \times 100\% = 18.5\% \tag{9}$$

where P_0 and P_{opt} are the estimated motion powers before and after topology-based reconstruction. Thus, the reported 18.5% reduction in motion power is consistent with the decrease in main-frame mass and the more efficient force-transmission path after reconstruction.

III. FINITE ELEMENT ANALYSIS

A. MODEL SIMPLIFICATION, MATERIAL PARAMETERS AND MESH INDEPENDENCE

Finite element analysis is conducted to evaluate strength, stiffness and dynamic reliability of the main load-bearing structure. The central frame, radial support legs and hinge connections are retained, while small bolts, gaskets and non-load-bearing details are simplified by equivalent connections. The main frame is modeled as 6061-T6 aluminum alloy with elastic modulus of 68.9 GPa, Poisson ratio of 0.33, density of 2700 kg/m3 and yield strength of 275 MPa. Joint-bearing components are treated as GCr15 bearing steel with elastic modulus of 206 GPa and Poisson ratio of 0.30. The modeling strategy follows the general idea of structural simplification and dynamic verification used in bionic continuous-structure and tracked pipeline-robot analyses [21]–[24].

The maximum-diameter condition is selected as the worst case because the support legs are fully extended and bending moment at the hinge root reaches its maximum. Radial constraints are applied at the contact pads to represent pipe-wall support, and driving torque and spring preload are applied according to the theoretical model. To avoid misleading interpretation of wheel-axle stress, the wheel/axle contact region is treated as an equivalent remote constraint rather than a detailed bearing-contact model. Therefore, any local stress concentration near the wheel-axis boundary in Figure 3 is regarded as a boundary-condition artifact and is not used as the design criterion. Mesh independence is checked by decreasing the characteristic element size until changes in maximum stress and deformation are below 2%. Mesh-independence verification of the finite element model is shown in Table 3.

The convergence curve in Figure 3a shows that both maximum stress and deformation approach stable values as the mesh is refined. When the element size decreases from 3.0 mm to 2.5 mm, the maximum stress changes from 186.4 MPa to 187.1 MPa (0.38%), and the maximum deformation changes from 0.523 mm to 0.526 mm (0.57%). Both variations are below the 2% criterion; therefore, the 3.0 mm mesh is adopted for subsequent static and modal simulations to balance accuracy and computational efficiency.

B. STATIC AND MODAL RESPONSE EVALUATION

Under the maximum-diameter working condition, the maximum Von-Mises stress of the main load-bearing frame is 186.4 MPa, which is lower than the yield strength of 6061-T6 aluminum alloy and gives a safety factor of about 1.47. The maximum deformation is 0.52 mm and occurs mainly at the end of the support leg, whereas the central frame remains nearly undeformed. Considering the simplified wheel/axis boundary treatment described in Section 3.1, the stress interpretation focuses on the hinge root and support-arm/base transition rather than the wheel-axis contact edge. The stress concentration at these structural locations is consistent with the cantilever-like force-transmission path of the radial support structure [25]–[27]. Modal analysis is used to check resonance risk. The undamped free-vibration equation is

$$([K] - \omega^2[M])\{\Phi\} = 0 \tag{10}$$

where $[K]$ is the stiffness matrix, $[M]$ is the mass matrix and Φ is the modal vector. The first six natural frequencies are 42.6, 68.3, 95.7, 127.4, 156.8 and 189.2 Hz. Since the typical working excitation frequency is 5–15 Hz, the first-order natural frequency is sufficiently separated from the operating band. Therefore, the structure has low resonance risk during normal cleaning and inspection tasks.

C. PROTOTYPE VERIFICATION AND EXPERIMENTAL GRANULARITY

To improve experimental granularity, a prototype verification index is defined for later strain-gauge and displacement tests. Strain gauges should be placed at the hinge root and support-arm transition, which are the stress-concentration regions predicted by FEA. The relative error between simulation and experiment is defined as

$$\epsilon = \frac{|\sigma_{\text{FEA}} - \sigma_{\text{exp}}|}{\sigma_{\text{FEA}}} \times 100\% \tag{11}$$

For EI-oriented validation, the target deviation should be controlled within 8% when comparing FEA stress with measured strain-derived stress. In addition, the cleaning module should be tested in pipes with oil sludge and shallow water. The wall-cleaning rate, slip ratio and current fluctuation can be used as quantitative indicators to verify the effectiveness of the elastic cleaning blade and hydrophobic structural design. Because the present manuscript mainly focuses on structural design and simulation, these tests are specified as the next experimental validation stage rather than claimed as fully completed measurements.

IV. TOPOLOGY-BASED WEIGHT REDUCTION AND MANUFACTURABLE RECONSTRUCTION

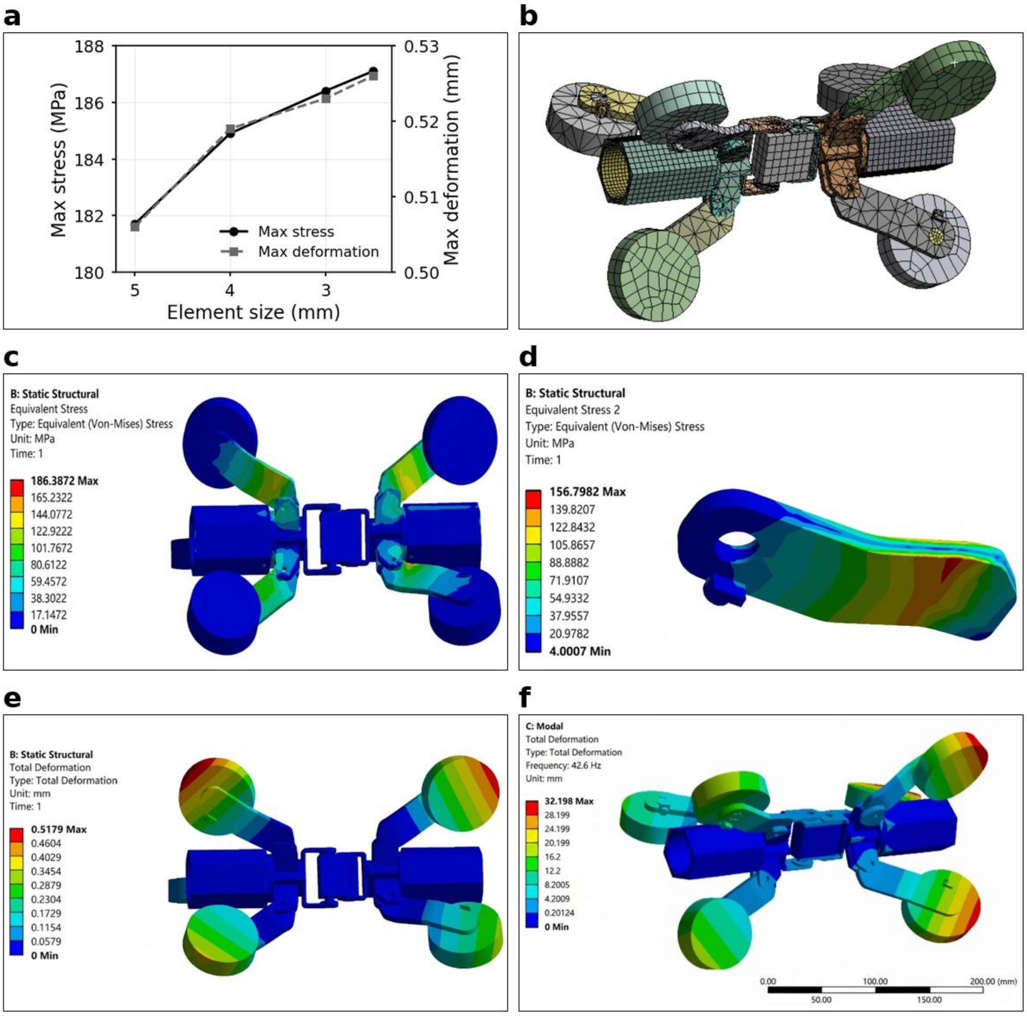

FIGURE 3. Mesh-independence verification, finite element and modal results. (a) Convergence of maximum stress and maximum deformation with element size. (b) Finite element mesh of the robot. (c) Overall Von-Mises stress distribution under static loading. (d) Local stress distribution of the support arm. (e) Total deformation distribution. (f) First-order modal deformation with natural frequency of 42.6 Hz. The wheel-axis region is modeled as an equivalent boundary/connection region, and local artifacts there are not taken as structural failure evidence.

A. SIMP OPTIMIZATION MODEL AND RECONSTRUCTION

Topology optimization is introduced to reduce the mass of the main frame while maintaining structural safety. To avoid overstating the result, the term “weight reduction” in this paper refers to the improvement from the initial structure to the reconstructed structure of the proposed robot, rather than a verified comparison with a deployed commercial product. The design domain includes the central frame and support-arm connection zones, while bearing holes, motor mounting surfaces and contact interfaces are defined as non-design regions. The variable-density SIMP method is adopted, and the elastic modulus of element e is interpolated by Eq. (12).

$$E_e(\rho_e) = E_{\min} + \rho_e^p (E_0 - E_{\min}) \tag{12}$$

where ρ_e is the relative material density, E_0 is the elastic modulus of solid material, $E_{\min}$ avoids singularity and p is the penalty factor. The optimization problem is formulated as Eq. (13).

$$\begin{aligned} \min \quad & C = F^T U \\ \text{s.t.} \quad & K(\rho)U = F, \quad V/V_0 \le 0.60, \\ & \sigma_{\max} \le [\sigma], \quad u_{\max} \le [u] \end{aligned} \tag{13}$$

The penalty factor is increased from 3.0 to 4.5 by the continuation method, the filter radius is set to 2.5 mm and convergence is reached after 45 iterations. The sensitivity of structural compliance to element density is calculated as

$$\frac{\partial C}{\partial \rho_e} = -p\rho_e^{p-1}(E_0 - E_{\min}) u_e^T k_0 u_e \tag{14}$$

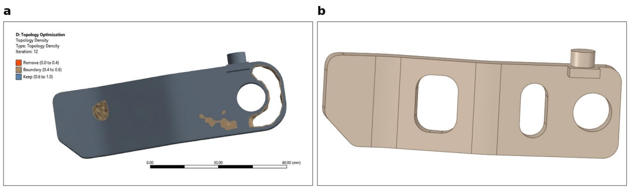

FIGURE 4. Topology optimization results retained from the original paper. (a) Material-density distribution of the optimized support component. (b) Reconstructed lightweight component after topology optimization.

TABLE 4. Within-design comparison before and after topology-based structural weight reduction.

Indicator	Before	After	Evaluation
Frame mass (kg)	2.84	2.17	-23.7%
Maximum stress (MPa)	186.4	158.7	safe
Maximum deformation (mm)	0.52	0.67	acceptable
Equivalent stiffness (N/mm)	2843	2695	-5.2%
Specific stiffness (N/(mm kg))	1001	1242	+24.1%
First-order frequency (Hz)	42.6	48.3	+13.4%
Motion power (W)	24.7	20.1	-18.5%

A small penalty factor leads to a large number of intermediate-density elements and blurred boundaries, whereas an excessively large value may cause oscillatory convergence. Therefore, the continuation strategy is adopted to obtain a stable solution and a clear 0-1 material distribution. For manufacturability, the irregular low-density regions are not directly machined. Instead, they are reconstructed as smooth variable-section beams and rounded lightening holes, while bearing holes, motor mounting surfaces and contact interfaces are retained as non-design regions. This conversion improves machining feasibility for aluminum alloy components and provides interfaces for potential carbon-fiber secondary parts. The resulting material-density distribution and reconstructed component are shown in Figure 4.

B. COMPARATIVE VERIFICATION OF LIGHTWEIGHT PERFORMANCE

After topology optimization, the main-frame mass decreases from 2.84 kg to 2.17 kg, corresponding to a reduction of 23.7% relative to the initial frame of the proposed robot. This comparison is useful for evaluating the effectiveness of the design iteration, but it is not equivalent to proving superiority over a mature commercial product. For product-level lightweighting, the same payload, pipe-diameter range, cleaning module and material system should be used as benchmark conditions. Therefore, Table 4 reports a within-design comparison, and the claim is worded as topology-based structural weight reduction. The optimized maximum stress is 158.7 MPa, still below the allowable stress. Although the equivalent stiffness decreases slightly, the specific stiffness increases because the mass reduction is larger than the stiffness loss. The first-order natural frequency increases to 48.3 Hz, indicating that the reconstructed load path is more efficient.

The comparison in Table 4 and Figure 5 indicates that

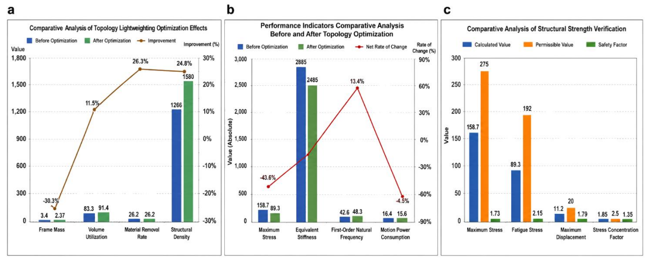

FIGURE 5. Performance comparison charts after topology-based structural weight reduction. a, Main-frame optimization effects. b, Mechanical-performance comparison before and after topology optimization. c, Comparative analysis of structural strength verification.

topology optimization removes redundant material from low-stress zones while retaining the main force-transmission path near hinge roots and connection nodes. In satisfying the strength requirement, the design achieves effective weight reduction within the proposed structure. However, comparison with a mature deployed robot should be carried out in future work using a normalized index such as mass per pipe-diameter coverage, payload-to-mass ratio or energy consumption per travelled distance.

V. CONCLUSIONS

This study proposes a bionic bone-contraction variable-diameter pipeline robot and completes structural design, bionic mapping, static/dynamic modeling, finite element verification and topology-based structural weight reduction. The main conclusions and innovations are as follows:

A cat-inspired six-leg radial variable-diameter mechanism is developed. The bionic principle is not limited to appearance imitation; it abstracts the feline shoulder-thorax compliance, scapular sliding and limb retraction into a flexible spine, universal joints, spring-preloaded support legs and servo-driven radial adjustment. This active-passive mechanism enables self-centering, impact buffering and continuous pipe-wall contact in 200–440 mm pipelines.

Static and dynamic models are established for variable-diameter operation. The calculated single-leg contact force is 5.40–5.77 N, the spring preload is 5.07–5.42 N and the minimum motor torque is 2.84–3.76 N m. The energy model explains the 18.5% reduction in motion power after lightweight reconstruction.

Finite element analysis verifies the structural safety. Under the worst working condition, the maximum Von-Mises stress is 186.4 MPa and the maximum deformation is 0.52 mm. The first-order natural frequency is 42.6 Hz, which is higher than the working excitation band.

SIMP-based topology optimization reduces the frame mass from 2.84 kg to 2.17 kg, corresponding to a 23.7% reduction relative to the initial frame. The optimized frame still satisfies strength and stiffness requirements and improves specific stiffness. This result should be interpreted as within-design topology-based weight reduction; product-level lightweight superiority should be verified by comparison with a mature robot under identical pipe-diameter, payload and material conditions.

The contribution of this work lies in the integration of bionic necessity analysis, expanded biological-to-mechanical mapping, active-passive variable-diameter adaptation, force-equilibrium modeling, dynamic energy analysis and topology-based structural weight reduction. The proposed method is especially suitable for small and medium municipal pipes because the robot can reduce its radial envelope in narrowed sections, recover support in enlarged sections, and maintain stable contact for cleaning and inspection. Future research should include a revised wheel-bearing/contact finite element model, strain-gauge validation with a target simulation-experiment error below 8%, oil-sludge and water-condition cleaning tests, and product-level benchmarking against mature pipeline robots.

DECLARATION OF CONFLICTING INTERESTS

The author(s) declared no potential conflicts of interest with respect to the research, author-ship, and/or publication of this article.

DATA SHARING AGREEMENT

The datasets used and/or analyzed during the current study are available from the corresponding author on reasonable request.

FUNDING

No funding was received for this work.

REFERENCES

[1] P. Wu, P. C. Huang, and J. L. Zhong, "Bionic micro surgical robot for medical targeted microvascular thrombolysis," J. Robot. Surg., vol. 3, p. 82, 2020.
[2] H. Gao, K. Jiang, M. Huang, et al., "Structural design and motion simulation of a new wheel-leg coordinated pipeline robot," Manuf. Autom., vol. 33, no. 13, pp. 15–19, 2011.
[3] S. Z. Zhang, D. Mu, Z. C. Cui, et al., "Dynamic analysis and simulation of a new expansion mechanism for pipeline cleaning robot," Mach. Build. Autom., vol. 46, no. 5, pp. 123–127, 2017.
[4] S. Z. Zhang, J. L. Huang, and Y. Q. Zheng, "Optimal design and simulation of unloading mechanism for improved pipeline dust cleaning robot," Min. Process. Equip., vol. 39, no. 1, pp. 121–125, 2011.
[5] L. N. Li, G. Z. Yan, P. P. Jiang, et al., "Design and experiment of micro bionic intestinal endoscope," Meas. Control Technol., vol. 32, no. 12, pp. 70–73, 77, 2013.
[6] Q. Lu, "Bionic crawling motion control of special pipeline robot," Technol. Wind, no. 16, p. 18, 2011.
[7] K. D. Wang, "Micro bionic robot for gastrointestinal examination," Sci. Technol. Vis., no. 26, pp. 65–68, 2023.
[8] Y. X. Zhao, J. J. Di, and D. W. Gao, "3D solid motion simulation of micro pipeline robot based on ADAMS," Res. Explor. Lab., vol. 30, no. 1, pp. 36–39, 2011.
[9] X. Liu, G. Q. Wang, J. Q. Gui, et al., "A new snake-like bionic wheel-leg pipeline inspection robot," Constr. Mach., no. 7, pp. 77–81, 2017.
[10] Z. L. Ye, L. A. Zhang, S. Sun, et al., "Design and analysis of bionic double-claw pipeline climbing robot," J. Mech. Sci. Technol., no. 6, pp. 81–89, 2024.
[11] J. Y. Gao, "Research on key technologies of micro bionic robot for intestinal examination," M.S. thesis, Shanghai Jiao Tong Univ., Shanghai, China, 2017.
[12] S. L. Yang, "Bionic design of magnetically responsive micro robot and its application in targeted therapy of in vivo lumens," M.S. thesis, Guangxi Univ., Nanning, China, 2025.
[13] Z. D. Jiao, "Research on key technologies of torsional soft actuator," Ph.D. dissertation, Zhejiang Univ., Hangzhou, China, 2021.
[14] D. L. Fang, B. L. Su, K. Y. Shao, et al., "Design and analysis of bionic flexible telescopic pipeline robot," Chin. Hydraul. Pneum., no. 10, pp. 103–111, 2025.
[15] X. R. Liu and X. X. Zhang, "Research and development of bionic driven soft pipeline detection robot," South. Agric. Mach., no. S1, pp. 157–159, 170, 2025.
[16] Q. P. Zhou, "Design and implementation of an intelligent inspection bionic robot for cable pipelines," Video Eng., no. 9, pp. 57–60, 70, 2022.
[17] C. Y. Liang, "Research on shape design of pipeline detection robot based on morphological bionics," M.S. thesis, Changchun Univ. Technol., Changchun, China, 2025.
[18] K. K. Cui and J. W. Yang, "Configuration design and kinematic simulation of a new pipeline port grinding robot," Weld. Pipe Tube, no. 4, pp. 44–48, 2019.
[19] Z. T. Li, "Analysis and design realization of bionic metamorphic working mechanism of a new knee exoskeleton robot," M.S. thesis, Tianjin Univ. Technol., Tianjin, China, 2025.
[20] Z. T. Li, Y. W. Yang, B. Li, et al., "A new bionic metamorphic knee exoskeleton robot and its multi-body motion scale synthesis method," J. Mech. Eng., vol. 59, no. 5, pp. 161–174, 2023.
[21] G. F. Jia, "Research on configuration design and motion characteristics of pipeline robot with bionic muscle structure," M.S. thesis, Tianjin Univ. Sci. Technol., Tianjin, China, 2024.
[22] P. Ning and W. S. Ding, "Kinematic analysis and simulation of micro pipeline flexible obstacle removal robot," J. Mach. Des. Manuf., no. 11, pp. 206–210, 216, 2023.
[23] P. Zhou, J. T. Yao, K. M. Zhu, et al., "Static analysis of bionic fishbone continuous robot based on Cosserat theory," Trans. Chin. Soc. Agric. Mach., vol. 54, no. 10, pp. 439–447, 2023.
[24] B. Z. Zhang, Z. Z. Wang, and C. X. Yang, "Dynamic analysis and simulation of diameter-varying mechanism of new tracked pipeline robot," J. Shijiazhuang Tiedao Univ. (Nat. Sci. Ed.), vol. 32, no. 4, pp. 65–69, 100, 2019.
[25] C. Tang, B. Du, S. Jiang, et al., "A pipeline inspection robot for navigating tubular environments in the sub-centimeter scale," Sci. Robot., vol. 7, no. 66, p. eabm8597, 2022.
[26] Y. Zhao, H. Huang, W. Yuan, et al., "Worm-inspired, untethered, soft crawling robots for pipe inspections," Soft Robot., vol. 11, no. 4, pp. 639–649, 2024.
[27] G. Blewitt, D. Cheneler, S. Monk, et al., "A review of worm-like pipe inspection robots: research, trends and challenges," Soft Sci., vol. 4, p. 13, 2024.